

1 **Mapping genetic effects on cell type-specific chromatin accessibility**
2 **and annotating complex trait variants using single nucleus ATAC-seq**

3
4 Paola Benaglio^{1,*}, Jacklyn Newsome^{2,*}, Jee Yun Han³, Joshua Chiou⁴, Anthony Aylward², Sierra
5 Corban¹, Mei-Lin Okino¹, Jaspreet Kaur¹, David U Gorkin³, Kyle J Gaulton^{1,5,#}

6
7 1. Department of Pediatrics, University of California San Diego, La Jolla CA 92093
8 2. Bioinformatics and Systems Biology Program, University of California San Diego, La Jolla CA
9 92093

10 3. Center for Epigenomics, Department of Cellular and Molecular Medicine, University of
11 California San Diego, La Jolla CA 92093

12 4. Biomedical Sciences Graduate Program. University of California San Diego, La Jolla CA
13 92093

14 5. Institute for Genomic Medicine, University of California San Diego, La Jolla CA 92093

15

16 * Authors contributed equally to this work

17

18 # Corresponding author:

19 Kyle Gaulton
20 9500 Gilman Drive, #0746
21 Department of Pediatrics
22 University of California San Diego
23 858-822-3640
24 kgaulton@ucsd.edu

25

26

27

28

29

30

31

32

33

34

35

36 **Abstract**

37

38 Gene regulation is highly cell type-specific and understanding the function of non-coding genetic
39 variants associated with complex traits requires molecular phenotyping at cell type resolution. In
40 this study we performed single nucleus ATAC-seq (snATAC-seq) and genotyping in peripheral
41 blood mononuclear cells from 10 individuals. Clustering chromatin accessibility profiles of
42 66,843 total nuclei identified 14 immune cell types and sub-types. We mapped chromatin
43 accessibility QTLs (caQTLs) in each immune cell type and sub-type which identified 6,248 total
44 caQTLs, including those obscured from assays of bulk tissue such as with divergent effects on
45 different cell types. For 3,379 caQTLs we further annotated putative target genes of variant
46 activity using single cell co-accessibility, and caQTL variants were significantly correlated with
47 the accessibility level of linked gene promoters. We fine-mapped loci associated with 16
48 complex immune traits and identified immune cell caQTLs at 517 candidate causal variants,
49 including those with cell type-specific effects. At the 6q15 locus associated with type 1 diabetes,
50 in line with previous reports, variant rs72928038 was a naïve CD4+ T cell caQTL linked to
51 *BACH2* and we validated the allelic effects of this variant on regulatory activity in Jurkat T cells.
52 These results highlight the utility of snATAC-seq for mapping genetic effects on accessible
53 chromatin in specific cell types and provide a resource for annotating complex immune trait loci.

54

55

56

57

58

59

60

61

62

63

64

65

66

67

68

69

70 **Introduction**

71

72 Genome-wide association studies have identified thousands of genomic loci associated with
73 complex human traits and disease^{1–3}, but their molecular mechanisms remain largely unknown.
74 Interpreting the mechanisms of trait-associated loci is paramount to an improved understanding
75 of the cell types, genes and pathways involved in complex traits and disease¹. Genetic variants
76 at complex trait-associated loci are primarily non-coding and enriched in transcriptional
77 regulatory elements^{1,4,5}, implying that the majority affect gene regulatory programs. As gene
78 regulation is highly cell type-specific^{6,7}, uncovering the molecular mechanisms of complex trait
79 loci requires determining the function of non-coding variants in the individual cell types that
80 comprise a tissue. While substantial advances have been made in annotating the non-coding
81 genome^{5,8}, the regulatory effects of genetic variants in specific cell types are still largely
82 unknown.

83

84 Mapping quantitative trait loci (QTLs) for molecular phenotypes such as gene expression levels,
85 histone modifications and chromatin accessibility is an effective strategy to determine the
86 regulatory activity of genetic variants^{9–15}. Molecular QTL studies to date have been primarily
87 performed in ‘bulk’ tissue, cell lines, or individual sorted cell types, however, and therefore have
88 not yet widely annotated the breadth of cell type effects. Single cell technologies have created
89 new avenues to study gene regulation in the specific cell types comprising a heterogeneous
90 tissue and define relationships to complex traits and disease^{16,17}. Several recent studies
91 mapped gene expression QTLs (eQTLs) using cell type-specific expression profiles derived
92 from single cell RNA-seq assays^{18–20}. These studies represented proof-of-concept for using
93 profiles derived from single cell data to map genetic effects on molecular phenotypes in specific
94 cell types and sub-types. Moreover, they enabled additional analyses which leveraged data
95 from across thousands of cells such as the identification of co-expression QTLs¹⁹. To date,
96 however, no studies have mapped chromatin accessibility QTLs in specific cell types and sub-
97 types using single cell assays.

98

99 In this study we used single nucleus ATAC-seq (snATAC-seq) to profile human peripheral blood
100 mononuclear cell (PBMC) samples. We derived chromatin accessibility profiles of immune cell
101 types and sub-types and mapped chromatin accessibility QTLs (caQTLs) for these profiles
102 which identified thousands of immune cell type and sub-type caQTLs. We characterized
103 caQTLs for each cell type, including caQTLs whose effects are obscured in bulk assays, and

104 linked distal caQTLs to putative target gene promoters using single cell co-accessibility. Finally,
105 we fine-mapped causal variants at genomic loci associated with 16 complex immune traits and
106 diseases, annotated fine-mapped variants for these traits with immune cell type caQTLs and
107 validated the molecular effects of high-probability caQTL variants.

108

109 **Results**

110

111 **Chromatin accessibility profiling of peripheral blood mononuclear cells**

112

113 We performed snATAC-seq and genotyping of human peripheral blood cell (PBMC) samples in
114 order to map genetic effects on lymphoid and myeloid cell type accessible chromatin (**Figure**
115 **1a**). We used droplet-based snATAC-seq (10X Genomics) to assay 10 PBMC samples from
116 individuals of self-reported European descent (**Supplementary Table 1, see Methods**). The
117 snATAC-seq libraries were sequenced to an average depth of 178M reads, and libraries had
118 consistently high-quality metrics including enrichment at transcription start sites (TSS) and
119 fraction of reads mapping in peaks (**Supplementary Table 2**). We then performed array
120 genotyping of each sample and imputed genotypes into 39.6M variants in the Haplotype
121 Reference Consortium (HRC) panel²¹. Principal components analysis of genotypes mapped
122 onto 1000 Genomes Project data confirmed European ancestry for the majority of samples
123 (**Supplementary Figure 1**).

124

125 After extensive quality control that removed low quality cells and potential doublet cells (**see**
126 **Methods**), we performed clustering of 66,843 snATAC-seq profiles, which revealed 14 clusters
127 (**Figure 1b**). We then assigned clusters to lymphoid and myeloid cell types and sub-types based
128 on the chromatin accessibility patterns at known marker genes (**Figure 1b, Supplementary**
129 **Figure 2, Supplementary Table 3**). For example, among immune cell types, *NCR1*
130 accessibility marked NK cells, *MS4A1* accessibility marked B cells, and *PCTRA* accessibility
131 marked plasmacytoid dendritic cells. Among cell sub-types, accessibility at *FOXP3* differentiated
132 regulatory T cells from other T cell sub-types, and accessibility at *TCL1A* differentiated naïve B
133 cells from memory B cells (**Supplementary Figure 2**). The proportion of each immune cell type
134 and sub-type was broadly consistent across samples (**Figure 1c, Supplementary Figure 3a**)
135 and was highly correlated with cell proportions determined from flow cytometry of cell surface
136 markers for each sample (**Supplementary Figure 3b-c**). Similarly, clusters were composed of
137 similar proportions of cells from different individuals (**Supplementary Figure 3d**). These results

138 demonstrate that snATAC of PBMCs resolved lymphoid and myeloid cell types and sub-types
139 with broadly consistent representation across samples.

140

141 **Mapping chromatin accessibility QTLs in immune cell types and sub-types**

142

143 Within each immune cell type and sub-type cluster, we aggregated reads for all cells in the
144 cluster, generated accessible chromatin read count profiles, and called accessible chromatin
145 sites using MACS2²². Considering all immune cell types and sub-types there were 210,771 total
146 accessible chromatin sites (**Supplementary Table 5**). Immune cell type and sub-type sites were
147 highly concordant with sites identified in a previous study of FACS-sorted immune cell types²³
148 (**Supplementary Figure 4**). We then performed QTL mapping of chromatin accessibility read
149 counts in these sites using RASQUAL²⁴, a method which combines population-based and allele-
150 specific mapping. We focused on the 5 immune cell types with appreciable numbers of cells (B,
151 CD4+ T, CD8+ T, monocyte, NK) and mapped QTLs at both cell type and sub-type resolution.
152 For each cell type or sub-type, we retained sites with >5 reads per sample on average and only
153 tested variants that mapped directly in accessible sites and were heterozygous in at least two
154 samples. After applying these filters, on average 67,979 variants per cell type were tested for
155 association with 46,373 peaks (3.8 variants/peak). For comparison, we also performed caQTL
156 mapping after merging all reads for each sample ignoring their cell of origin to mimic a 'bulk'
157 ATAC-seq experiment.

158

159 In total we identified 6,248 distinct caQTLs in an immune cell type or sub-type (at FDR <0.1),
160 including 5,187 at cell type resolution and 5,398 at sub-type resolution (**Figure 2a**,
161 **Supplementary Table 6**). We also identified 5,697 caQTLs at 'bulk' resolution (**Figure 2a**,
162 **Supplementary Table 6**). There was limited evidence for reference bias in the resulting
163 caQTLs (1.68% with $\psi < .25$, annotated in **Supplementary Table 6**). Excluding the allelic
164 imbalance component from QTL mapping resulted in substantially fewer caQTLs at FDR<.10
165 (168 cell type, 426 sub-type) although the allelic effects were highly concordant
166 (**Supplementary Figure 5**). The majority of caQTLs were identified at FDR<.10 at different
167 resolutions, although a subset was found only at one resolution (**Figure 2a**). The number of
168 caQTLs identified in each cell type was proportional to the number of cells for that cell type
169 (**Figure 2b**), likely due to differences in available read depth leading to reduced power for less
170 common cell types. Most caQTLs were identified at FDR<.10 in only one cell type or sub-type
171 (80% for cell types, 75% for cell sub-types) (**Figure 2c**). However, when considering caQTLs

172 significant in at least one cell type, allelic effects (π) were strongly correlated across cell types
173 as well as with 'bulk' data (median Spearman correlation $r=0.63$, **Figure 2d**), with stronger
174 correlation between more similar cell types.

175

176 We next compared cell type caQTLs in our study to external QTL datasets previously generated
177 in immune cells. We first compared caQTL results from our 'bulk' analysis with caQTLs
178 previously mapped in 24 lymphoblastoid cell lines (LCLs)²⁴. Of the 2,694 caQTLs in our data
179 that were tested in the LCL study, 660 (24.4%) were also significant LCL caQTLs (OR=15.9,
180 $P<2.2\times10^{-16}$, Fisher's exact test) of which 164 shared also the same lead variant (OR=4.2,
181 $P=1.05\times10^{-16}$ Fisher's exact test) and were 99.99% concordant in their effect direction (**Figure**
182 **2e**). Of note, when considering caQTLs from each individual cell type, B cell caQTLs had the
183 highest overlap with LCL caQTLs, consistent with LCLs being derived from B cells
184 (**Supplementary Figure 6**). We next compared caQTLs in our study to published histone
185 H3K27ac QTLs (hQTLs) and expression QTLs (eQTLs) from FACS-sorted T cells and
186 Monocytes from the BLUEPRINT project¹⁵. The enrichment for T cell hQTLs was stronger in
187 CD4+ (OR=3.8, $P=3.2\times10^{-113}$, Fisher's exact test) and CD8+ (OR=3.4, $P=1.3\times10^{-60}$) T cell
188 caQTLs compared to monocyte caQTLs (OR=1.6, $P=9.1\times10^{-16}$) (**Figure 2f**). We observed the
189 converse pattern for monocyte hQTLs, which were more enriched for monocyte caQTLs than T
190 cell caQTLs (CD4+ T cell OR=1.65, $P=3.8\times10^{-20}$; CD8+ T cell OR=1.7, $P=1.4\times10^{-18}$; monocyte
191 OR=2.4, $P=1.1\times10^{-153}$) (**Figure 2f**). We observed the same cell type enrichment pattern for T
192 cell and monocyte eQTLs (T-cell eQTLs: CD4+T-cell OR=1.51, $P=1.2\times10^{-42}$; CD8+ T cell
193 OR=1.3, $P=5.6\times10^{-14}$; monocyte OR=1.2, $P=2.0\times10^{-15}$; monocyte eQTLs: CD4+ T cell OR=1.2,
194 $P=2.4\times10^{-10}$; CD8+ T cell OR=1.2, $P=1.4\times10^{-8}$; monocyte OR=1.3, $P=3.9\times10^{-39}$, **Figure 2f**).
195

196

196 To identify transcription factors (TFs) mediating immune cell type caQTLs, we identified TF
197 sequence motifs preferentially disrupted by caQTL variants in each cell type. We used
198 MotifBreakR²⁵ to predicted allelic effects of SNPs on TF motifs from the HOCOMOCO v10
199 human database²⁶, comprising 640 motifs corresponding to 595 unique TFs. We first predicted
200 allelic motif effects for all variants tested for QTL association. Then, for each TF motif, we
201 compared the proportion of motif instances disrupted by caQTLs compared to non-caQTL
202 variants. Thus, we were able to measure the enrichment of predicted TF-disrupting caQTLs for
203 each TF motif. Immune cell type caQTLs were broadly enriched for disrupting any TF motif
204 compared to non-caQTL variants (OR=1.2, $P=6.1\times10^{-4}$, Fisher's exact test). When considering
205 caQTLs in each cell type, there were 25 TF motifs significantly enriched for B cell caQTLs, 44

206 motifs enriched for CD4+ T cell caQTLs, 29 motifs enriched for CD8+ T cell QTLs, 29 motifs
207 enriched for NK cell QTLs and 93 motifs enriched for monocyte QTLs (FDR<0.05, one-tailed
208 binomial test, **Figure 2g, Supplementary Table 7**). Motifs disrupted by caQTLs included those
209 with broadly shared enrichment across different cell types including ETS1, ETV6 and GABP1,
210 as well as those with highly cell type-specific enrichment such as BCL11A in B cells (FDR=
211 0.012), SPI1 in B cells and monocytes (FDR=3.07x10⁻⁸, FDR=5.10x10⁻³⁴), and CEBPB in
212 monocytes (FDR=7.8x10⁻¹⁷).

213
214 At numerous loci, caQTLs mapped at cell type and sub-type resolution provided insight beyond
215 those obtained by mapping caQTLs in bulk tissue. The most straightforward examples consisted
216 of caQTLs for accessible chromatin sites active in only one cell type, where the effects of a
217 caQTL identified in bulk data could be simply ascribed to that cell type (1,776 caQTLs,
218 **Supplementary Figure 7a**). For example, rs13294415 was a caQTL for a B cell-specific site
219 (allelic effects π =.79, q-value=.003), rs11136478 was a caQTL for a CD4+ T cell-specific site
220 (π =.65, q=.013), rs10888395 was a caQTL for a monocyte-specific site (π =.31, q=2.1x10⁻⁴) and
221 rs1475159 was a caQTL for a NK cell-specific site (π =.81, q=6.3x10⁻⁴) (**Figure 2h**). We also
222 identified caQTLs for immune sub-type-specific sites (1,325 caQTLs), such as rs3014874 which
223 was a caQTL for a classical monocyte-specific site (π =.28, q=.008) and rs7094953 which was a
224 caQTL for a naïve CD4+ T cell-specific site (π =.26, q=.008) (**Supplementary Figure 7b**).
225 Another class of caQTLs were those for sites active in all cell types, yet where the variant
226 effects were specific to only a few cell types (2,362 and 2,704 for cell types and subtypes,
227 respectively). For example, variant rs61943586 mapped in a site active in all immune cell types
228 and had a significant effect in CD8+ T cells (π =.76, q=1.4x10⁻⁴), but no effect in B cells and
229 monocytes (π =.50, q=.96; π =.48, q=.76) (**Figure 2i**). Similarly, variant rs747748 mapped in a
230 site active in all cell types yet only had a significant effect in classical monocytes (π =.43,
231 q=.0018) (**Supplementary Figure 7c**). In these latter examples, variant effects in bulk data
232 were dampened due to the inclusion of cell types with no effect (rs61943586 bulk π =.57, q=.04;
233 rs747748 bulk π =.48, q=.18) (**Figure 2i, Supplementary Figure 7c**).

234
235 We also observed caQTLs with more complex effects, such as those with divergent effects on
236 different cell types (41 and 60 for cell types and subtypes, respectively). In one example, variant
237 rs1867687 was a significant caQTL in all immune cell types, where the G allele had increased
238 accessibility in B cells and monocytes (B cell π =.66, q-value=.02; monocyte π =.66, q=4.8x10⁻⁴)

239 and the A allele had increased accessibility in CD4+ and CD8+ T cells and NK cells (CD4+ T
240 $\pi=.29$, $q=.002$; CD8+ T $\pi=.20$, $q=.001$; NK cell $\pi=.27$, $q=.064$) (**Figure 2j**). In comparison,
241 rs1867687 had no effect in 'bulk' data ($\pi=.51$, $q=.78$). The alleles of this variant were predicted
242 to bind different TFs, where the G was predicted to bind SPI1 and SPIB motifs and the A allele
243 was predicted to bind IRF TF motifs (**Figure 2k**). SPI1 and SPIB motifs were specifically
244 enriched in B cells and monocytes, whereas IRF motifs were broadly enriched across cell types
245 (**Figure 2k**), suggesting a potential mechanism through which this variant has opposing effects
246 on different immune cell types.

247

248 **Linking distal caQTLs to effects on target gene promoters**

249

250 Among the 6,248 caQTLs identified in our study, a minority (17%) mapped to gene promoter
251 regions. The remaining caQTLs were in chromatin sites distal to promoters, and we therefore
252 sought to define the target genes of these caQTLs. Co-accessibility between pairs of accessible
253 chromatin sites across single cells has been used to annotate putative target genes of distal
254 enhancers^{17,27}. We therefore defined co-accessible sites (co-accessibility score $>.05$) in the 5
255 immune cell types with $>1k$ cells (CD4+ T, CD8+ T, B, monocyte, NK) using Cicero²⁷. For each
256 cell type we retained co-accessible sites greater than 10kb apart and that also were co-
257 accessible in at least two samples individually. In total we identified 481,963 pairs of co-
258 accessible sites, which included between 75k and 132k per cell type (**Figure 3a**). We compared
259 co-accessible sites for each cell type to chromatin interactions from promoter capture Hi-C
260 (pCHi-C) data previously generated in 16 immune cell types and sub-types²⁸. We observed
261 strongest enrichment of cell type co-accessible sites for the corresponding cell type in pCHi-C
262 interactions in each case, except for NK cells, which were not assayed by pCHi-C (**Figure 3b**).
263 When segregating co-accessible sites by distance, there remained strong enrichment for pCHi-
264 C interactions even at distances of up to 1MB (**Figure 3c**).

265

266 Using the co-accessible sites identified for each cell type we then annotated caQTLs with their
267 putative target genes. There were 179,347 distal accessible chromatin sites co-accessible with
268 at least one promoter site (30.5k-44.4k per cell type) and 66,571 promoter sites co-accessible
269 with promoter sites of a different gene (13.0k-18.1k per cell type) (**Figure 3d-e**). Across all
270 6,248 caQTLs, 3,379 were either in a site co-accessible with at least one gene promoter or in a
271 promoter site directly. Among these 3,379 caQTLs, the majority were distal sites co-accessible

272 with a promoter (54-65% per cell type) (**Figure 3f**. Among distal caQTLs co-accessible with a
273 gene promoter, 38-53% were linked to just one gene (**Figure 3g**).

274
275 Previous studies have identified coordinated allelic effects between distal sites and interacting
276 promoters²⁹. We therefore tested caQTL variants for association with chromatin accessibility
277 levels of all promoter sites co-accessible with the caQTL site. There was a positive and highly
278 significant correlation between variant allelic effects on the original site and effects on co-
279 accessible promoter sites (B $r=.24$, CD4+ T $r=.23$, CD8+ T $r=.16$, monocyte $r=.21$, NK $r=.17$,
280 Pearson correlation) (**Figure 3h**). When separating co-accessible sites by distance, the
281 correlations were reduced between more distal sites (**Supplementary Figure 8**). As we were
282 unable to leverage allelic imbalance in this analysis, our power was more limited, and we only
283 identified 7 linked promoter caQTLs at FDR<.20 (**Figure 3i**). There was a significant, positive
284 correlation in variant effects on the linked promoter caQTL and the original caQTL (**Figure 3i**).
285 For example, at the 6p24 locus rs4959438 was a caQTL for a distal site in B cells ($\pi=.65$,
286 $q=.0066$) and was also a caQTL for the *DSP* promoter linked to the distal site ($\pi=.59$, $q=.077$)
287 (**Figure 3j**). This variant was also a QTL for the expression of *DSP* in whole blood in GTEx v8⁹
288 ($NE=29$, $P=3.2 \times 10^{-12}$), and which was directionally consistent with the C allele having
289 increased activity. Together these results demonstrate how snATAC-seq data can be used to
290 link caQTLs to effects on putative target genes.

291
292 **Identifying caQTLs at fine-mapped variants for complex immune trait loci**
293
294 Genomic loci affecting complex immune traits and disease are primarily non-coding, and the
295 causal variants and molecular mechanisms at these loci are largely unknown. We therefore
296 used immune cell type and sub-type caQTLs to annotate variants associated with complex
297 immune traits and disease. We first collected published genome-wide association summary
298 statistics for 16 blood cell count, autoimmune, inflammatory and allergy traits imputed into
299 reference panels with comprehensive variant coverage such as 1000 Genomes or the
300 Haplotype Reference Consortium (**Figure 4a, Supplementary Table 8**). At most traits, fine-
301 mapping of causal variant sets at associated loci was either not performed as part of the initial
302 study or not made publicly available. We therefore fine-mapped primary association signals at
303 loci reported for these 16 traits using a Bayesian approach, from which we generated credible
304 sets of variants representing 99% of the total posterior probability for each signal (**see Methods**,
305 **Supplementary Data 1**). Across all traits there were 1,275 total credible sets, which contained

306 a median of 16 variants, where traits with the smallest credible set sizes included monocyte
307 count (median 6.5 variants), basophil count (median 7.5 variants) and rheumatoid arthritis
308 (median 9 variants). At 396 signals fine-mapping resolved credible sets to 5 or fewer variants
309 (**Figure 4a**).
310

311 A total of 523 credible set variants representing 211 association signals were immune cell type
312 or sub-type caQTLs (**Figure 4b**). We determined whether fine-mapped variants for each trait
313 were preferentially enriched for caQTLs from specific immune cell sub-types by comparing to a
314 background of non-caQTL sites (**see Methods**). The majority of traits (12/16) showed nominal
315 enrichment ($P<.05$) for caQTL peaks in at least one immune cell sub-type, several of which
316 recapitulated known biology of cell types contributing to the trait (**Figure 4c**). For example, type
317 1 diabetes (T1D)-associated variants were enriched in CD4+ T cell caQTLs (naïve CD4+ T
318 logOR=1.9, $p=0.024$; activated CD4+ T logOR=1.5, $p=0.043$), where T cells are the critical cell
319 type in the pathogenesis of T1D³⁰. Lymphocyte count-associated variants were enriched in
320 caQTLs for lymphocyte cell types (memory B logOR=2.9, $p=0.024$; naïve CD4+ T logOR=1.7,
321 $p=0.012$). Strong enrichments for other traits may similarly point to cell types involved in trait
322 biology. For example, child onset asthma-associated variants were enriched in activated CD4+
323 T cells (logOR=2.5, $p=0.001$) and memory B cells caQTLs (logOR=4.1, $p=0.001$) (**Figure 4c**),
324 and ulcerative colitis-associated variants were strongly enriched in classical monocyte caQTLs
325 (logOR=2.6, $p=0.001$).
326

327 Among fine-mapped variants that were immune cell caQTLs, 185 had a posterior probability
328 >1% and were either in a distal site linked to a gene promoter or in a promoter site directly
329 (**Figure 4d, Supplementary Table 9**). Among these, at multiple loci fine-mapped variant
330 caQTLs replicated cell type-specific effects observed in previous studies^{31,32}. For example, at
331 the 5q11.2 locus associated with rheumatoid arthritis (RA), among the two candidate variants
332 with highest causal probability rs28722705 (PPA=.70) and rs7731626 (PPA=0.28) only
333 rs7731626 mapped in an accessible chromatin site (**Supplementary Figure 9a**). This variant
334 was a caQTL in naïve CD4+ T cells ($\pi=0.38$, $q=0.06$), and was co-accessible with the *IL6ST* and
335 *ANKRD55* promoters (**Supplementary Figure 9b-e**). A previous study identified rs7731626 as
336 likely causal for multiple sclerosis and RA and was also a T cell-specific eQTL for both *IL6ST*
337 and *ANKRD55*³¹. At the 15q22.33 locus, rs17293632 was fine mapped in multiple traits
338 including Crohn's disease (PPA=.28) and asthma (PPA=.16), and was a monocyte caQTL
339 ($\pi=.40$, $q=.0138$) which was co-accessible with the promoter of multiple SMAD3 isoforms

340 (Supplementary Figure 9f-i). The high effect C allele of rs17293632 was also predicted to
341 have allele-specific binding to a JUN/FOS TF family motif, which were specifically enriched in
342 monocyte caQTLs (Supplementary Figure 9j, Figure 2g).

343

344 In another example, at the 6q15 locus associated with type 1 diabetes (T1D) and multiple other
345 traits, rs72928038 (PPA=.07) was a caQTL in naïve CD4+ T cells ($\pi=0.26$, $q=4.9\times 10^{-3}$) where
346 the reference and T1D-protective allele G had increased accessibility (Figure 4e-f). The site
347 harboring rs72928038 was specific to naïve CD4+ T cells and was co-accessible with multiple
348 gene promoters including *BACH2* (Figure 4e, Supplementary Table 9). The G allele was also
349 predicted to have allele-specific binding to ETS family motifs, which were broadly enriched
350 among T cell caQTLs (Figure 4g). We validated the allelic effects of this variant on regulatory
351 activity using reporter assays in Jurkat T cells. There were significant effects on enhancer
352 activity in luciferase gene reporter assays where the G allele had increased activity (Two-sided
353 t-test, $P=.015$), and allele-specific transcription factor binding to the G allele in electrophoretic
354 mobility shift assays (Figure 4h). Previous studies have shown that this variant is a QTL in
355 CD4+ T cells³¹, and this site was linked to the *BACH2* promoter in promoter-capture Hi-C data in
356 naïve CD4+ T cells²⁸.

357

358 We next identified caQTLs for high-probability fine-mapped variants at loci without established
359 molecular mechanisms. At the 11q23 locus associated with child-onset asthma, we fine-mapped
360 a single variant rs12365699 to near-causality (PPA=.98) (Figure 4i, Supplementary Table 9).
361 This variant was a caQTL in activated CD4+ T cells, effector CD8+ T cells and memory B cells,
362 where the reference and risk-increasing allele G had higher accessibility (CD4+ T $\pi=0.36$,
363 $q=5.4\times 10^{-4}$, CD8+ T $\pi=0.33$, $q=6.5\times 10^{-3}$, B $\pi=0.35$, $q=0.073$, respectively) and was linked to the
364 promoter regions of multiple genes including *CXCR5* and *NLRX1*, the latter of which is ~300kb
365 distal to the variant (Figure 4i,j). The G allele of rs12365699 was also predicted to have allele-
366 specific binding for *ZSCAN16* (Figure 4k). At the 12p13.33 locus associated with lymphocyte
367 count, we also fine mapped a likely causal variant rs34038797 (PPA =.94), which had the same
368 effect in all cell sub-types (strongest association in classical monocytes $\pi=0.26$, $q=9.2\times 10^{-4}$) and
369 was co-accessible with multiple genes (Supplementary Figure 10a-c). The C allele had higher
370 accessibility and higher predicted affinity with ETS transcription factors, which were ubiquitously
371 enriched in immune cell caQTLs (Supplementary Figure 10d).

372

373

374 **DISCUSSION**

375

376 In this study we demonstrated that profiles derived from single nucleus ATAC-seq assays can
377 be used to map chromatin accessibility QTLs in individual cell types, even with modest sample
378 sizes. While we profiled only a small number of samples in our study, we identified thousands of
379 immune cell type and sub-type caQTLs. A likely contributor to the large number of caQTLs we
380 identified despite the small sample is the high depth at which samples were sequenced, which
381 provides greater power for allelic imbalance mapping. Supporting this, we identified few caQTLs
382 when performing population-based QTL mapping only. As the number of unique reads covering
383 a variant can in theory be much higher for snATAC-seq compared to bulk ATAC-seq due to the
384 thousands of unique libraries per assay, the value of snATAC-seq compared to bulk ATAC-seq
385 in mapping allelic imbalance is even more pronounced. Deeply sequenced snATAC-seq assays
386 even in few samples therefore represent an effective approach to map genetic effects on
387 chromatin profiles from multiple cell types in a heterogeneous tissue.

388

389 Mapping caQTLs at cell type resolution enabled insights into cell type-specific regulation that
390 are obscured from assays of bulk tissue chromatin. For example, we identified variants mapping
391 in sites active in all cell types but with allelic effects on only a few cell types. We also identified
392 examples of variants with opposite effects on different cell types resulting in no net effect in
393 bulk. In both of these scenarios, simply annotating bulk caQTLs using reference maps of cell
394 type-specific chromatin sites would not be sufficient to uncover these effects, and therefore
395 requires mapping accessible chromatin profiles in each cell type directly. Single cell data also
396 enabled additional cell type-specific analyses such as linking distal sites to putative target gene
397 promoters using co-accessibility²⁷. While high-resolution maps of distal 3D interactions exist for
398 many immune cell types in promoter-capture Hi-C²⁸, most other tissues do not currently have
399 such cell type-resolved interaction maps and therefore cell type co-accessibility data will be
400 particularly valuable in annotating distal caQTLs in these tissues.

401

402 Although we mapped thousands of immune cell type caQTLs from few snATAC-seq samples,
403 our study design also has several notable limitations. Most importantly, there was a large
404 difference in the number of caQTLs per cell type or sub-type dependent on the number of cells
405 assayed. For example, we identified few significant caQTLs for the less common sub-types
406 identified in our data such as adaptive NK cells and memory B cells. There are even further sub-
407 divisions of immune cell types that we were not able to identify due to the resolution of snATAC-

408 seq profiles. As identifying caQTLs from rarer cell types and sub-types will therefore require
409 many additional snATAC-seq assays to sufficiently define their profiles, cell sorting may
410 represent a more efficient and cost-effective strategy at present for QTL mapping in these cell
411 types. An additional limitation of our study was that, due to the small number of samples
412 profiled, we focused only on variants mapping in accessible chromatin sites directly in order to
413 leverage allelic imbalance. As we did not test all variants at a locus for association to each site,
414 we had limited ability to formally compare caQTL association and disease association signals,
415 for example using colocalization techniques³³. Moving forward studies profiling larger sample
416 sizes and cell numbers will help circumvent these limitations. Furthermore, data from multiomic
417 assays of joint gene expression and accessible chromatin will help resolve cell types and sub-
418 types and facilitate joint caQTL and eQTL mapping³⁴.

419

420 In summary, we identified thousands of caQTLs in immune cell type and sub-types from
421 peripheral blood samples using single cell chromatin accessibility assays. Immune cell caQTLs
422 mapped to hundreds of loci associated with complex immune traits and disease and therefore
423 represent a valuable resource for interpreting the molecular mechanisms of these loci. Given
424 the ability to deconvolute individual cells into their sample-of-origin²⁰, one promising strategy
425 moving forward will be to pool samples prior to running snATAC-seq assays, which will reduce
426 the per-sample cost and facilitate studies of greater genotype diversity. Mapping cell type-
427 specific chromatin exposed to disease-relevant conditions and stimuli will also help uncover the
428 breadth of genetic effects^{23,35}. Together these efforts will enable more comprehensive
429 annotation of variant function in human cell types and their contribution to complex disease.

430

431 **METHODS**

432

433 **Single nuclei ATAC-Seq**

434 Peripheral blood mononuclear cells (PBMCs) from 10 individuals (4 females and 6 males) were
435 purchased from HemaCare (Northridge, CA) and profiled for snATAC using 10x Genomics
436 Chromium Single Cell ATAC Solution, following manufacturer's instructions (Chromium
437 SingleCell ATAC ReagentKits UserGuide CG000209, Rev A) as described previously¹⁷. Briefly,
438 cryopreserved PBMC samples were thawed, resuspended in 1 mL PBS (with 0.04% FBS) and
439 filtered with 50 µm CellTrics. Cells were centrifuged and permeabilized with 100 µl of chilled
440 lysis buffer (10 mM Tris-HCl pH 7.4, 10 mM NaCl, 3 mM MgCl₂, 0.1% Tween-20, 0.1%
441 IGEPAL-CA630, 0.01% digitonin and 1% BSA) for 3 min on ice and then washed with 1mL

442 chilled wash buffer (10 mM Tris-HCl pH 7.4, 10 mM NaCl, 3 mM MgCl₂, 0.1% Tween- 20 and
443 1% BSA). After centrifugation, pellets were resuspended in 100 μ L of chilled Nuclei buffer
444 (2000153, 10x Genomics) in a final concentration of 3,000 to 7,000 of nuclei per μ L. 15,300
445 nuclei (targeting 10,000) were used for each sample. Tagmentation was performed using nuclei
446 diluted to 5 μ L with 1X Nuclei buffer, 10x ATAC buffer and ATAC enzyme from 10x Genomics,
447 for 60 min at 37°C. Single cell ATAC-seq libraries were generated using the Chromium Chip E
448 Single Cell ATAC kit (10x Genomics, 1000086) and indexes (Chromium i7 Multiplex Kit N, Set
449 A, 10x Genomics, 1000084) following manufacturer instructions. Samples were sequenced to
450 an average depth of 178 million 50-nt read pairs each, using an illumina HiSeq4000 instrument
451 at the UCSD Institute for Genomic Medicine. Alignment to the hg19 genome and initial
452 processing were performed using the 10x Genomics Cell Ranger ATAC v1.1 pipeline. We
453 filtered reads with MAPQ<30, secondary or unmapped reads, and duplicate reads from the
454 resulting bam files using samtools³⁶. Sample information and a summary of the Cell Ranger
455 ATAC-seq quality metrics are provided in **Supplementary Table 1**.

456

457 **Quality control, clustering and cell type assignment**

458 For each sample we performed multiplet removal ($N_{\text{cells}}=1,311$) using Cell Ranger's custom
459 multiplet removal script (version 1.1). The genome was split into 5 kb windows and windows
460 overlapping blacklisted regions from ENCODE (version 2) were removed. For each sample, a
461 sparse $m \times n$ matrix containing read depth for m cells (identified using the snATAC-seq
462 barcodes) passing read depth thresholds at n windows was then generated.

463

464 Initial cell clustering was performed separately for each snATAC-seq sample sparse matrix
465 using scanpy (version 1.5). Highly variable windows were extracted using mean read depths
466 and dispersion was normalized. Read depth was normalized, and the log-transformed read
467 depth was regressed out for each cell. Principal component analysis was then performed, and
468 the top 50 principal components were used to calculate the nearest 30 neighbors using the
469 cosine metric. This cosine metric was then used to perform UMAP dimensionality reduction
470 clustering with the parameters 'min_dist=0.3', along with further sub-clustering using the
471 Louvain clustering algorithm with the parameters 'resolution=1.25'. Clusters with a low fraction
472 of reads in promoter, a low log usable read count, and/or a low fraction of reads in peaks were
473 iteratively removed for each sample ($N_{\text{cells}}=6,333$). The samples filtered for low quality cells were
474 then merged, and PCs and UMAP dimensions were obtained as above and Harmony was used
475 to correct for donor batch effects³⁷. Manual doublet removal was then performed by removing

476 Louvain-defined sub-clusters that had higher than average useable read counts, mapped
477 between clusters and/or expressed multiple marker genes. Clusters that did not have uniform
478 representation across samples were also removed. A total of 14,268 cells were removed during
479 all of the quality control steps. UMAP dimensionality reduction was performed again using the
480 same parameters on the remaining cells in order to re-cluster a final time.

481

482 In order to assign cell type and sub-type identity to each cluster, we determined chromatin
483 accessibility at 5 kb windows around promoter regions of known marker genes (see
484 **Supplementary Table 3**).

485

486 **Peak Calling**

487 For each cluster mapped reads were extracted from all cells within the cluster. Reads
488 aligning to the positive strand were shifted by +4 bp and reads aligned to the negative
489 strand were shifted by -5 bp. Reads were extended to 200 bp and then centered, and bed
490 files were created from the resulting read coordinates. We then called peaks with MACS2²² from
491 the bed files using the parameters ‘-q 0.05’, ‘-nomodel’, ‘-keep-dup all’, ‘-g hs’, and ‘-B’. The
492 read count pileup bedgraph was sorted and normalized to counts per million (CPM), converted
493 to bigwig and visualized using the UCSC Genome Browser. We created a merged peak set by
494 combining narrow peak files across all cell type and sub-type clusters into a single bed file.

495

496 **Comparison with bulk immune cell ATAC-seq data**

497 We obtained published data of FACS-sorted immune cell types (GSE118189)²³, mapped reads
498 to hg19 using bwa mem³⁸ and removed duplicate reads. We merged replicate samples and
499 performed peak calling for each cell type as described above. Mapped reads from immune cell
500 types and sub-types derived from snATAC-seq in this study and from the bulk immune cell
501 ATAC-seq profiles were used to generate bedgraph files using bedtools³⁹. Read counts were
502 normalized to CPM and bigwig files were generated using ENCODE ‘bedgraphToBigWig’⁴⁰. We
503 created a bed file of the union of peak calls from snATAC-seq and bulk ATAC-seq using
504 bedtools. We then compared bulk ATAC-seq cell type and snATAC-seq cell type normalized
505 read count profiles within the union peak set using deeptools ‘multiBigWigSummary’⁴¹. A
506 heatmap of the clusters of Spearman rank correlation coefficients indicating similarity between
507 bigwig files was generated using deeptools ‘plotCorrelation’ and the summary comparison from
508 ‘multiBigWigSummary’.

509

510 **Sample genotyping and imputation**

511 Genomic DNA from PBMC samples was extracted using the PureLink genomic DNA kit
512 (Invitrogen). Genotyping was performed using Infinium Omni2.5-8 arrays (Illumina) at the UCSD
513 Institute for Genomic Medicine. Genotypes were assigned with GenomeStudio (v.2.0.4) with
514 default settings. Variants with minor allele frequency (MAF) < 0.01 or with ambiguous alleles
515 (G/C, or A/T) and MAF > 0.4 were filtered out using PLINK. For the remaining variants, we
516 imputed genotypes into the Haplotype Reference Consortium (HRC) r1.1 panel using the
517 Michigan Imputation Server with minimac4. We then retained variants with imputation quality
518 R2>0.7

519

520 **Identification of chromatin accessibility QTLs**

521 For each sample, we split reads in the snATAC .bam files according to cluster label. For each
522 cell type and sub-type cluster, we generated peak count matrices (peak x sample) using merged
523 peak site coordinates and the split .bam files using featureCounts⁴². We then obtained VCF
524 files of SNPs located within peaks and annotated allelic read counts using RASQUAL tools²⁴.
525 We filtered for variants heterozygous in at least 2 samples. For the 'bulk' experiment we
526 ignored cell type labels and used all reads.

527

528 For each cell type and sub-type, we retained only accessible sites with at least 5 reads on
529 average across samples. To perform caQTL analysis we used RASQUAL and tested for
530 association between each peak and variants contained in the peak itself or in other peaks within
531 a 10Kb window. We included the library size of each sample calculated using the
532 rasqualCalculateSampleOffsets() function and read count covariates using make_covariates()
533 function in each model. The number of ATAC-seq read count covariates were dynamically
534 calculated for each cell type and sub-type and therefore different cell types/sub-types had
535 different numbers of covariates. We also included the first four principal components derived
536 from genotype data together with major 1KG populations as covariates in each model.

537

538 For each peak, we calculated adjusted p-values accounting for the number of variants tested
539 per peak, and the variant with the minimum adjusted p-value was marked as the lead variant.
540 To correct for multiple testing genome-wide, we performed permutations of labels across
541 samples and counts across alleles of heterozygous variants. For the permutations across
542 samples, we required that the labels were swapped within the samples of European and

543 American ancestry separately. We then repeated the association tests and calculated an
544 empirical FDR (10%) by comparing the q-values of the real and permuted association results.

545
546 To estimate the correlation of effect sizes of caQTLs across cell types and 'bulk' data we
547 calculated the spearman correlation coefficient of effect sizes (π) in each pair of cell types and
548 "bulk". For each comparison we selected lead SNP-peak pairs that were significant caQTLs in at
549 least one of the two cell types. Correlation coefficients were tabulated in a matrix and
550 hierarchically clustered using 'pheatmap'. Bulk-like caQTLs were compared with caQTLs from
551 24 LCLs also calculated using RASQUAL²⁴. Of 172,241 peaks tested in PBMCs, 65,787
552 intersected with a peak tested in LCLs, and 660 were caQTLs in both dataset (FDR 10%).
553 Enrichment was estimated using Fisher's exact test. To calculate coordination of caQTLs effects
554 we restricted the analysis to those peaks having the same lead variants (589), 164 of which
555 were caQTLs in both datasets. Monocyte and CD4+ and CD8+ T-cells single-cell caQTLs were
556 compared with H3K27ac QTLs and eQTLs from FACS sorted Monocytes and T-cells from the
557 BLUEPRINT project, calculated using WASP and the Combined Haplotype Test at FDR 10%,
558 which similarly to RASQUAL takes into account both allelic and population effects. For each
559 comparison we selected variants tested in both datasets and calculated enrichment for shared
560 variant QTLs (lead variants only) using Fisher's exact test.

561
562 **Transcription factor motif analysis**

563 To identify enriched motifs that were altered by caQTLs we used the package MotifBreakR²⁵.
564 First, we selected 109,554 SNPs that were tested in any of the cell types for caQTLs and
565 imported them using the function snps.from.file(), using hg19 as reference genome. Then we
566 determined if they disrupted TF motifs from the HOCOMOCO v10 human database²⁶,
567 comprising 640 motifs corresponding to 595 unique TFs, and accessed via MotifDb. The
568 following motifbreakR() function parameters were used: filterp = TRUE, method="ic", = 5e-4,
569 BPPARAM = BiocParallel::bpparam("SerialParam"). SNPs that resulted in disruption of any TF
570 motif with a *strong* effect (defined by motifbreakR) were considered as motif altering
571 (n=107,280). To calculate enrichment for alteration of specific TF in caQTLs of individual cell
572 types (B-cell, CD4_T-cell, CD8_T-cell, NK_cell, Monocyte), we performed a one-tailed exact
573 binomial test (binom.test(alternative= "greater")) comparing the frequency of alteration of a motif
574 by caQTLs to the total frequency of motif alteration in the tested SNPs for each cell type.
575 Significant enrichment was considered at a Benjamini & Hochberg corrected P-value<0.05. To

576 display enriched motifs we used the packages MotIV and motifPiles, selecting the top motifs in
577 each cell type ranked by p-value.

578

579 **Single cell co-accessibility**

580 Peak-to-peak co-accessibility was calculated using Cicero (version 1.1.5)²⁷ for B-cells, CD4+ T-
581 cells, CD8+ T-cells, NK cells, and Monocytes. We created a sparse binary matrix encoding the
582 snATAC-seq barcodes for each cell in a given cell type and the superset of ATAC-seq peaks for
583 all cell types, indicating which cells were accessible in which peaks. For each cell type, the
584 cicero function 'make_cicero_cds' was used to aggregate cells into bins of 30 nearest neighbors
585 (parameter k=30) from the UMAP reduced dimensions obtained from clustering. We then
586 calculated co-accessibility scores using a window size of 1 Mb. Once co-accessibility scores
587 were calculated, a threshold of 0.05 and a minimum distance of 10 kb were used to define pairs
588 co-accessible for a given cell type. We also generated cell type co-accessibility for each sample
589 individually and only retained sites co-accessible at .05 in at least two individual samples. A
590 peak was categorized as 'promoter' if it fell within a 2 kb window of a transcription start site
591 based on GENCODE (version 19) promoter annotations⁴³, and otherwise was categorized as
592 'distal'.

593
594 To validate the cell-type specificity of promoter-distal sites connections calculated using co-
595 accessibility, we compared them to chromatin interactions from promoter capture Hi-C (pCHi-C)
596 data previously generated in 16 immune cell types and sub-types²⁸. We obtained the list of
597 promoter baits and the matrix containing CHiCAGO scores for all interactions in all immune cell
598 type. First, for each pair of peaks that we analyzed in each cell type, we filter those where at
599 least one peak intersected (+/- 1kb) a pCHi-C bait using pglttools⁴⁴. Then, we identified
600 overlapping connection between the filtered pairs of sites in each of our 5 cell type (B-cells,
601 CD4+ T-cells, CD8+ T-cells, NK cells, and Monocytes) and the pCHi-C connection (CHiCAGO
602 score >= 5) from each of the 16 blueprint adult cell types (Mon, Mac0, Mac1, 'Mac2', Neu, MK,
603 EP, Ery, nCD4, tCD4, aCD4, naCD4, nCD8, tCD8, nB, tB) using the function
604 compare_connections() from the Cicero package. For each celltype-celltype comparison we
605 then estimated the enrichment for the co-accessible sites in pCHi-C connection using Fisher's
606 exact test. Odds ratios for each comparison were tabulated and displayed using heatmap. For
607 each of the matching cell types (B-cells-tB, CD4+T-cells-tCD4, CD8+T-cells-'tCD8', and
608 Monocytes-Mon) we also calculated enrichment at different peak distances (10-50, 50-100, 100-
609 200, 200-350, 350-1000 kb).

610

611 **Distal effect of caQTL variants on coaccessible-promoters**

612 To examine the effect of caQTLs on co-accessible sites, for each of the 5 major cell types we
613 took the lead caQTL variant and tested for association with accessibility level of the co-
614 accessible site using RASQUAL²⁴. We used the same method as above for caQTLs with the
615 exception of adopting a more relaxed FDR threshold of 20% instead of 10%. caQTLs-
616 coaccessible peaks were then filtered to retain only enhancer-promoters and promoter-promoter
617 co-accessible peaks (B-cells n=828, CD4+ T-cells n=2,323, CD8+ T-cells n=1,909, NK cells
618 n=1,489, Monocytes n=2,243, with an average number of 3.45 co-accessible promoters for
619 each caQTL). Pearson correlation of effect sizes was calculated between variant effect on the
620 original caQTL peak and on one of the co-accessible promoters (with lowest RASQUAL p-value
621 of association), and only considering co-accessible peaks at >10kb of distance.

622

623 **Genetic fine mapping analysis**

624 We obtained genome-wide summary statistics for immune-related phenotypes including blood
625 cell type counts⁴⁵, autoimmune diseases⁴⁶⁻⁵⁰, and inflammatory diseases⁵¹⁻⁵³. For each study,
626 we obtained lists of index variants for each independent signal from the supplement. We used
627 PLINK⁵⁴ to estimate linkage disequilibrium (LD) between these index variants and all variants
628 within ± 2.5 Mb using samples of European ancestry from the 1000 Genomes Project⁵⁵. For
629 each signal, we first pre-filtered variants in at least low LD ($r^2 > 0.1$) with the index variants. We
630 calculated approximate Bayes factors⁵⁶ (aBF) for each variant using the effect estimates (β) and
631 standard errors (SE), assuming prior variance $w=0.04$. We calculated the posterior probability of
632 association (PPA) by dividing the aBF for each variant by the sum of aBFs for all variants
633 included in the signal. We then defined the 99% credible set as the smallest set of variants that
634 added up to 99% PPA. Fine-mapped variants were annotated using cell type and sub-type
635 caQTLs, considering each lead variant as well as variants with the same q-value of the lead
636 variant for each caQTL. Fine-mapped caQTL variants with PPA > 1% were then further
637 annotated with co-accessible promoters (**Supplementary Table 8**).

638

639 To test for enrichment of caQTLs for complex immune traits we calculated the cumulative PPA
640 of variants overlapping immune cell sub-type caQTL peaks across all credible sets for each trait.
641 For each cell sub-type, we defined a background set of peaks tested for association but did not
642 have significant caQTLs. We estimated an empirical distribution for the total PPA using 1,000
643 random draws of peaks from the background equal in number to the caQTL sites. For each test

644 (trait vs cell sub-type) a p-value was calculated by comparing the total PPA within caQTL peaks
645 to the empirical distribution.

646

647 **Luciferase gene reporter assays**

648 Human DNA sequences (Coriell) with reference allele for rs72928038 (*BACH2* intron) were
649 cloned in forward orientation in the luciferase reporter vector pGL4.23 (Promega) using the
650 primers: forward, AGCTAGGTACCACTCAGTGGTGGGTTT, and reverse,
651 TACCAGAGCTCCTGGATAGAGGTCCCAGTCG and the enzymes SacI and KpnI. Alternate
652 allele plasmids were generated via site directed mutagenesis (Q5 SDM kit, New England
653 Biolabs) using the following primers: forward, CGGATTCCCTaTAAGCTGATC, reverse,
654 TCCCTATTGTGTGTAATG.

655

656 Jurkat cells were maintained in culture at a concentration of 1×10^5 /mL- 1×10^6 /mL.
657 Approximately 0.5×10^6 cells per replicate (3 replicates) were co-transfected with 500 ng of
658 firefly luciferase vector containing either the reference or alternate allele or an empty pGL4.23
659 vector as a control, and 50 ng pRL-SV40 Renilla luciferase vector (Promega), using the
660 Lipofectamine LTX reagent. Cells were collected 48 hours post transfection and assayed using
661 the Dual-Luciferase Reporter system (Promega). Firefly activity was normalized to the Renilla
662 activity and expressed as fold change compared to the luciferase activity of the empty vector
663 (RLU). A two-sided t-test was used to compare the luciferase activity between the two alleles.

664

665 **Electrophoretic mobility shift assays**

666 EMAs were performed according to manufacturer's instruction, with changes indicated below,
667 using the LightShift™ Chemiluminescent EMSA Kit (Thermo Scientific, 20148). Biotinylated and
668 non-biotinylated single-stranded oligonucleotides harboring the rs72928038 variant (5'-
669 TAGGGACGGATTCCTGTAAGCTGATCTTGAAG-3', 5'-
670 TAGGGACGGATTCCTATAAGCTGATCTTGAAG-3') were purchased from Integrated DNA
671 Technologies. Nuclear extract from E6-1 Jurkat T cells (ATCC TIB-152), cultured as described
672 above, was obtained using the NE-PER Nuclear and Cytoplasmic Extraction Reagents (Thermo
673 Scientific, 78833). Binding reactions were carried in a total volume of 20 μ l, with 10X Binding
674 Buffer (100 mM Tris pH 7.5, 500 mM KCl and 10 mM DTT), 2.5% glycerol, 5 mM MgCl₂, 0.05%
675 NP40, 50 ng Poly(dI:dC), 100 fmole of biotin-labeled probe, and 5.1 μ g nuclear extract. For
676 competition experiments, 20 pmol of unlabeled probe was added. Competition reactions were

677 incubated at room temperature for 10 mins before the addition of the biotin-labeled probe. At the
678 addition of the biotin-labeled probe, all reactions were incubated at room temperature for 20
679 min. Reactions were loaded onto a 6% polyacrylamide 0.5X TBE Gel (Invitrogen,
680 EC62655BOX) for electrophoresis and transferred for 45 mins to a Biodyne™ B Pre-Cut
681 Modified Nylon Membrane, 0.45 μ m (Thermo Scientific, 77016). Transferred DNA was UV-
682 crosslinked for 15 mins, and the biotinylated probes were detected using Chemiluminescent
683 Nucleic Acid Detection Module (Thermo Scientific, 89880) following the manufacturers
684 instruction, with initial blocking increased to 60 mins. The image was acquired using C-DiGit
685 Blot scanner (LI-COR Biosciences, Model 3600).

686

687 **FIGURE LEGENDS**

688

689 **Figure 1. Single nucleus ATAC-seq in a population of PBMC samples.** a) Schematic
690 overview of the study. b) Clustering of single cell accessible chromatin profiles of 66,843
691 PBMCs from 10 individuals. Cells are plotted based on the first two UMAP components.
692 Fourteen distinct clusters, indicated by different colors, were identified and assigned to a cell
693 type based on known marker genes. The number of cells for each cell type is indicated in
694 parenthesis. c) Barplot showing the relative proportions of each cell type in each sample. Color
695 scheme is the same as in 1b.

696

697 **Figure 2. Identification and characterization of immune cell type chromatin accessibility**
698 **QTLs.** a) Venn diagram showing the total number of caQTLs from single-cell ATAC-seq across
699 immune cell types (red), cell sub-types (blue); and in 'bulk' (gray). b) Number of caQTLs
700 identified in each cell type (red for cell types, blue for sub-types) and the subset found in 'bulk'
701 data (gray). c) Number of caQTLs unique or common to different cell types. d) Heatmap of
702 pairwise correlation (Spearman) between effect sizes of caQTLs, where association is
703 significant in at least one of the two cell types in the pair. e) Comparison between caQTLs from
704 PBMC bulk-like data and published caQTLs from 24 LCLs. Venn diagram on top indicates the
705 number of significant caQTLs in each dataset and their overlap. Scatter plot of effect sizes for
706 caQTLs found in both studies and having the same lead variant. f) Overlap between cell type
707 caQTLs and H3K27ac QTLs (top) or gene expression QTLs (bottom) in either Monocytes (gray)
708 or T cells (black). g) Top transcription factor motifs disrupted by caQTL variants across different
709 cell types. Clustering is based on motif similarity. The heatmap shows the enrichment ranking of
710 each TFs in each cell type. h) Examples of caQTLs in peaks specific to a single cell type

711 including rs13294415 (B cell-specific), rs1475159 (CD4+ T cell-specific), rs10888395
712 (Monocyte-specific) and rs11136478 (NK cell-specific). Top panels: colored-coded box-plots
713 show association in the different cell types, white box-plots show caQTL in 'bulk' PBMCs.
714 Association q-values are shown on the top and variant genomic location (hg19) is shown at the
715 bottom. Bottom panels: genome-browser screenshot of cell type chromatin profiles. i) Variant
716 rs61943586 was in peaks active in all cell types but was a significant caQTL in CD8+ T cells
717 only. Left: genome-browser screenshot of cell type chromatin signal. Right: boxplots as in H. I)
718 Variant rs1867687 was a significant caQTL in all cell types but had opposite effects in different
719 cell types. Top-left: genome-browser screenshot of cell type chromatin signal. Top-right: boxplot
720 of signal split by genotype in bulk and each cell type. Boxplots are color-coded as in I. Bottom-
721 left: TF motifs altered by the rs1867687 variant and their respective score differences are
722 shown. Positive scores indicate preference for alternate allele. Bottom-right: UMAP plot showing
723 accessibility of the SPI1 gene in Monocytes and B-cells and ubiquitous accessibility of IRF1.
724

725 **Figure 3. Linking distal immune cell caQTLs to putative target genes.** a) Number of co-
726 accessible links in each immune cell type. b) Enrichment of cell type co-accessible links for
727 overlap with promoter-capture Hi-C (pcHi-C) interactions in immune cell types. c) Enrichment of
728 cell type co-accessible links for pcHi-C interactions separated by distance between linked sites.
729 d) Number of co-accessible links between a promoter site (+/- 1kb) and a distal (non-promoter)
730 site in each cell type. e) Number of co-accessible links between promoter sites. f) Breakdown of
731 caQTLs linked to promoters in each cell type, including caQTLs directly in promoter sites,
732 caQTLs in distal sites co-accessible with a promoter site, caQTLs in promoter sites co-
733 accessible with a different promoter site, and more complex cases involving multiple linked
734 caQTLs. g) Breakdown of caQTLs in each cell type by the number of promoter sites they were
735 linked to. h) Correlation in the effects of caQTL variants on the primary site and co-accessible
736 promoter sites in each cell type. Pearson correlation coefficient and number of co-accessible
737 pairs of peaks are indicated. i) Correlation in caQTL variant effects on the primary site and co-
738 accessible promoter site for variants significant (FDR 20%) for the latter. j) A caQTL in B cells
739 rs4959438 was also a QTL for a co-accessible site at the *DSP* promoter and an eQTL for *DSP*
740 in GTEx.

741
742 **Figure 4. Immune cell type caQTLs at fine-mapped complex immune trait loci.** a) Fine-
743 mapping of causal variants at association signals for 16 complex immune traits and diseases.
744 Bar plots represent the number of variants in credible sets for each trait. b) Posterior

745 probabilities of caQTLs at fine-mapped variants for each immune trait and disease. c). d)
746 Breakdown of caQTLs for fine-mapped variants that were linked to promoter sites. e) Regional
747 plot of the locus on chr6 near *BACH2* associated with type 1 diabetes (T1D). (top) T1D variant
748 association, with credible set variants highlighted in red, (bottom) chromatin signal in naïve
749 CD4+ T cells and the co-accessible link between the site harboring rs72928038 and the *BACH2*
750 promoter. f) Cell type-specific effects of rs72928038 on naïve CD4+ T cell chromatin. (top)
751 Chromatin signal grouped by rs72928038 genotype in bulk PBMCs and naïve CD4+ cells on
752 top, (bottom) genome browser of chromatin signal in each cell type. g) Predicted TF sequence
753 motifs at rs72928038, where the variant base is highlighted. h) Validation of allelic activity for
754 rs72928038 in T cells. (top left) Luciferase gene reporter of sequence surrounding the G and A
755 allele of rs72928038 in Jurkat T cells. The G allele had significantly higher reporter activity. (top
756 right) Electrophoretic mobility shift assay of oligonucleotides containing the G and A allele of
757 rs72928038 in Jurkat T cells, where the G allele had protein binding. i) Regional plot of the
758 chr11 locus near *CXCR5* associated child asthma. (top) Asthma association statistics, with the
759 two credible set variants highlighted in red, (bottom) chromatin signal in activated CD4+ T cells
760 and the co-accessible links between the site harboring rs12365699 and the *CXCR5*, *BCL9L*,
761 *NLRX1*, *MCAM*, and *MPZL3* promoters. j) Cell type-specific effects of rs12365699. (top)
762 Chromatin signal grouped by rs12365699 genotype in bulk PBMCs and activated CD4+ cells on
763 top, (bottom) genome browser of chromatin signal in each cell type. k) Predicted TF sequence
764 motifs at rs12365699, where the variant base is highlighted.

765

766 **SUPPLEMENTARY FIGURE LEGENDS**

767

768 **Supplementary Figure 1. Population structure of PBMC samples.** The first four principal
769 components derived from joint analysis of genotype data from the 1000 Genomes Project and
770 PBMC samples. Samples in 1000 Genomes are colored by major population group, and the
771 PBMC samples are colored in pink.

772

773 **Supplementary Figure 2. Defining immune cell types and sub-types from snATAC-seq**
774 **profiles.** a) UMAP plots showing promoter accessibility in a 1 kb window around the TSS for
775 selected cell type marker genes (see Supplementary Table 3). b) Genome browser plots
776 showing aggregate read density (scaled to uniform 1×10^5 read depth, range: 5-35, shown on
777 vertical axis for each plot) for cells within each cell type for selected cell type marker genes.

778

779 **Supplementary Figure 3. Immune cell type snATAC-seq profiles in individual PBMC**
780 **samples.** a) UMAP plot showing cells clustering in each of the 10 PBMC samples assayed in
781 this study. b) Scatter plot comparing cell type proportions obtained from cluster analysis versus
782 those obtained from flow cytometry, excluding leukocytes. Proportions represent the fraction of
783 all cells in each sample (see Supplementary Table 4 for individual sample proportions). Each
784 dot represents an individual sample. c) Barplot showing the number of cells assigned to 14
785 distinct immune cell types and sub-types in each sample. d) Barplot showing the relative
786 proportion of cells from each sample in each immune cell type and sub-type.

787

788 **Supplementary Figure 4. Comparison of ATAC-seq peaks from PBMC snATAC and FACS**
789 **sorted PBMCs.** Heatmaps and hierarchical clustering of Spearman correlation coefficients for
790 pairwise comparisons of genome-wide ATAC-seq profiles across (a) cell-types or (b) sub-types
791 from PBMC snATAC from this study (in blue) and from a published bulk ATAC-Seq study using
792 FACS sorted immune cells (in black).

793

794 **Supplementary Figure 5. Comparison of caQTL effects with and without the allelic**
795 **imbalance component.** For each cell type (first 5 plots) and cell sub-type (remaining 10 plots),
796 a scatter plot show the consistency between caQTL effect considering both allelic and
797 population effect (x-axis) and the effect for the same variant-peak pair using only the population
798 component (y-axis) obtained running RASQUAL using the --population-only option. The
799 percentage of discordant effect are indicated.

800

801 **Supplementary Figure 6. Comparison of snATAC-seq caQTLs with LCL caQTLs from 24**
802 **individuals.** a-e) Significant PBMC caQTLs in a) B-cells, b) CD4+ T-cells, c) CD8+ T-cells, d)
803 Monocytes and e) NK-cells and their overlap with caQTLs from LCLs (Venn diagram,
804 considering only peaks tested in both datasets. For each shared caQTLs between each cell
805 type and LCLs, a scatter plot shows effect sizes for caQTLs found in both studies and having
806 the same lead variant. f) Table with p-values and odds ratio from two-tailed Fisher's exact test
807 for enrichment of cell-type caQTLs in LCLs caQTLs.

808

809 **Supplementary Figure 7. Examples of caQTLs specific to immune sub-types.** a) Examples
810 of cell-type specific caQTLs due to presence of the peak in a single cell type. From left to right,
811 rs1957554 is a caQTL for a naïve B cell-specific site, rs7094953 is a caQTL for a naïve CD4+ T
812 cell-specific site, rs3014874 is a caQTL for a classical monocyte-specific site, and rs59176853

813 is a caQTL for a cytotoxic NK cell-specific site. Top panels: colored-coded box-plots show
814 association in the different cell types, white box-plots show corresponding caQTL in bulk
815 PBMCs. Association q-values are shown on the top and variant genomic location (hg19) is
816 shown at the bottom. Bottom panels: genome-browser screenshot of snATAC-seq in different
817 cell types. b) Example of caQTL specific to classical monocytes (rs747748) although the peak is
818 active in all immune cell types. Box-plots show association with the same variant in 10 immune
819 sub-types and the bulk PBMCs. Right: genome-browser screenshot of cell-type color-coded
820 snATAC-seq peaks and position of the variant. c) Example of a caQTL specific to effector CD8+
821 T cells (rs61943586) although the peak is active in all cell types.

822

823 **Supplementary Figure 8. Correlation of caQTL effects with effects at distal promoters**
824 **across different distances.** Correlation in the effects of caQTL variants on the QTL site and
825 co-accessible promoter sites in each cell type, grouped by distance between the QTL site and
826 co-accessible promoter site. Pearson correlation coefficient and number of co-accessible pairs
827 of peaks are indicated.

828

829 **Supplementary Figure 9. Additional examples of immune cell type caQTLs at fine-**
830 **mapped complex immune trait loci with cell-specific effect.** a) Regional plot of a locus on
831 chr5 associated with rheumatoid arthritis, with the four credible set variants highlighted in red.
832 The candidate causal variant rs7731626 is indicated with a triangle and PPA. b) Chromatin
833 signal in naïve CD4+ T cells in the region and co-accessible link between the site harboring
834 rs7731626 and the *IL6ST* (aka *GP130*) promoter. The other three peaks co-accessible with
835 rs7731626 map to the promoter of a non-coding isoform of *ANKRD55* (in green). c) Zoomed-in
836 chromatin signals at the rs7731626 and the *IL6ST* promoter sites in all cell subtypes, showing
837 specificity for naïve CD4+ T cells. d) Chromatin signal at the rs7731626 variant grouped by
838 rs7731626 genotype in bulk PBMCs and naïve CD4+ cells and q-values of association. e) Top
839 four predicted TF sequence motifs rs7731626, where the variant base is highlighted. Twelve
840 other motifs predicted to be altered are not shown. f) Regional plot of the locus on chr15
841 associated with Crohn's disease, with the five credible set variants highlighted in red. The
842 candidate causal variant rs17293632 is indicated with a triangle and PPA. g) Chromatin signal
843 in classical monocytes in the region and co-accessible link between the intronic enhancer
844 harboring rs17293632 and three alternative *SMAD3* promoters. h) Zoomed-in chromatin signals
845 at the rs17293632 (right) and *SMAD3* promoter sites in all cell subtypes, showing specificity for
846 monocytes at the enhancer site and the two closest promoters. i) Chromatin signal at the

847 enhancer site grouped by rs17293632 genotype in bulk PBMCs, monocytes (including all
848 subtypes), classical monocytes and non-classical monocytes, with q-values of association
849 (RASQUAL). j) Four predicted TF sequence motifs rs7731626, where the variant base is
850 highlighted. Ten other similar motifs (ETS family) predicted to be altered are not shown.

851

852 **Supplementary Figure 10. Additional examples of immune cell type caQTLs at fine-**
853 **mapped complex immune trait loci with high causal probability.** a) Regional plot of the
854 locus on chr12 in the *NINJ2* gene showing association with Lymphocyte count, with the eight
855 credible set variants highlighted in red. The candidate causal variant rs34038797 is indicated
856 with a triangle and its PPA is shown. b) Chromatin signal in memory CD8+ T cells and Classical
857 Monocytes in the same region and the co-accessible link between the site harboring
858 rs34038797 and promoters of *CCDC77*, *WNK1*, *RAD52* (CD8+ T), *NINJ2* and *SLC6A12*
859 (Monocyte). c) Chromatin signal at the rs34038797 variant grouped by rs34038797 genotype in
860 all cell sub-types and q-values of association (RASQUAL) and zoomed-in genome browser
861 track. d) Top five predicted TF sequence motifs altered by rs34038797, where the variant base
862 is highlighted.

863

864 **SUPPLEMENTARY TABLES**

865

866 **Supplementary Table 1. Summary of PBMC samples information.** For each of the 10
867 samples analyzed, sample name, lot number, donor ID, donor age, gender, ethnicity, blood
868 type, and flow cytometry markers percentages are indicated.

869

870 **Supplementary Table 2. Summary of snATAC-seq cell ranger statistics.** For each of the 10
871 samples analyzed, we indicate snATAC-seq sequencing and mapping statistics.

872

873 **Supplementary Table 3. Marker genes references.** List of marker genes used to assign
874 clusters to PBMC cell types and sub-types and corresponding reference papers.

875

876 **Supplementary Table 4. Clustering vs. flow cytometry cell type proportions.** Comparison
877 between cell type proportions in each sample as estimated by flow cytometry and snATAC.

878

879 **Supplementary Table 5. Immune cell type and sub-type accessible chromatin sites.**

880 Merged bed file of all ATAC peaks sites called in each cell type and sub-type, used for all
881 analyses.

882

883 **Supplementary Table 6. Immune cell type and sub-type caQTLs.** RASQUAL results for all
884 caQTLs significant at FDR 10% in each cell type (5 cell types and 10 sub-types) and pseudo-
885 bulk analyses. The first 25 columns are outputs from RASQUAL, and p-values and q-values
886 were calculated from columns 11 and 10, respectively.

887

888 **Supplementary Table 7. Transcription factor motifs enriched in immune cell type caQTLs.**

889 List of TF motifs from the HOCOMOCO v.10 human database that were tested for enrichment in
890 caQTLs and results of binomial test.

891

892 **Supplementary Table 8. Complex immune traits and diseases included in fine-mapping.**

893 List of traits and corresponding GWAS study used for fine mapping.

894

895 **Supplementary Table 9. Immune cell type and sub-type QTLs at fine-mapped variants.**

896 List of SNPs in credible sets for blood and auto-immune traits that are caQTLs in one or more
897 cell types, have PPA >0.01 and are located either in gene promoters or in enhancers that are
898 co-accessible with distal promoters. For each fine-mapped variant we report caQTL results and
899 co-accessible promoters (multiple entries) in each of the cell types with significant caQTLs.

900

901 **SUPPLEMENTARY DATA FILES**

902

903 **Supplementary Data 1. Summary statistics of caQTLs in PBMC cell types, subtypes, and**
904 **bulk like data.** RASQUAL results for all peaks tested in each cell type (5 cell types and 10 sub-
905 types) and pseudo-bulk analyses. The first 25 columns are outputs from RASQUAL, and p-
906 values and q-values were calculated from columns 11 and 10, respectively.

907

908 **Supplementary Data 2. Fine-mapping credible sets for loci associated with 16 complex**
909 **immune traits.** The 99% credible sets derived from fine-mapping of loci associated with 16
910 complex immune traits and disease.

911

912

913 1. Claussnitzer, M. *et al.* A brief history of human disease genetics. *Nature* **577**, 179–189
914 (2020).

915 2. Manolio, T. A. *et al.* Finding the missing heritability of complex diseases. *Nature* **461**,
916 747–753 (2009).

917 3. Buniello, A. *et al.* The NHGRI-EBI GWAS Catalog of published genome-wide association
918 studies, targeted arrays and summary statistics 2019. *Nucleic Acids Res.* **47**, D1005–D1012
919 (2019).

920 4. Maurano, M. T. *et al.* Systematic localization of common disease-associated variation in
921 regulatory DNA. *Science* **337**, 1190–1195 (2012).

922 5. ENCODE Project Consortium. An integrated encyclopedia of DNA elements in the human
923 genome. *Nature* **489**, 57–74 (2012).

924 6. Kim-Hellmuth, S. *et al.* Cell type-specific genetic regulation of gene expression across
925 human tissues. *Science* **369**, (2020).

926 7. Meuleman, W. *et al.* Index and biological spectrum of human DNase I hypersensitive
927 sites. *Nature* **584**, 244–251 (2020).

928 8. ENCODE Project Consortium *et al.* Expanded encyclopaedias of DNA elements in the
929 human and mouse genomes. *Nature* **583**, 699–710 (2020).

930 9. GTEx Consortium. The GTEx Consortium atlas of genetic regulatory effects across human
931 tissues. *Science* **369**, 1318–1330 (2020).

932 10. GTEx Consortium *et al.* Genetic effects on gene expression across human tissues. *Nature*
933 **550**, 204–213 (2017).

934 11. Degner, J. F. *et al.* DNase I sensitivity QTLs are a major determinant of human expression
935 variation. *Nature* **482**, 390–394 (2012).

936 12. Li, Y. I. *et al.* RNA splicing is a primary link between genetic variation and disease.
937 *Science* **352**, 600–604 (2016).

938 13. McVicker, G. *et al.* Identification of genetic variants that affect histone modifications in
939 human cells. *Science* **342**, 747–749 (2013).

940 14. Khetan, S. *et al.* Type 2 Diabetes-Associated Genetic Variants Regulate Chromatin
941 Accessibility in Human Islets. *Diabetes* **67**, 2466–2477 (2018).

942 15. Chen, L. *et al.* Genetic Drivers of Epigenetic and Transcriptional Variation in Human
943 Immune Cells. *Cell* **167**, 1398–1414.e24 (2016).

944 16. Watanabe, K., Umićević Mirkov, M., de Leeuw, C. A., van den Heuvel, M. P. & Posthuma,
945 D. Genetic mapping of cell type specificity for complex traits. *Nat. Commun.* **10**, 3222 (2019).

946 17. Chiou, J. *et al.* Single cell chromatin accessibility reveals pancreatic islet cell type- and
947 state-specific regulatory programs of diabetes risk.
948 <http://biorkiv.org/lookup/doi/10.1101/693671> (2019) doi:10.1101/693671.

949 18. Cuomo, A. S. E. *et al.* Single-cell RNA-sequencing of differentiating iPS cells reveals
950 dynamic genetic effects on gene expression. *Nat. Commun.* **11**, 810 (2020).

951 19. van der Wijst, M. G. P. *et al.* Single-cell RNA sequencing identifies celltype-specific cis-
952 eQTLs and co-expression QTLs. *Nat. Genet.* **50**, 493–497 (2018).

953 20. Kang, H. M. *et al.* Multiplexed droplet single-cell RNA-sequencing using natural genetic
954 variation. *Nat. Biotechnol.* **36**, 89–94 (2018).

955 21. McCarthy, S. *et al.* A reference panel of 64,976 haplotypes for genotype imputation.
956 *Nat. Genet.* **48**, 1279–1283 (2016).

957 22. Zhang, Y. *et al.* Model-based analysis of ChIP-Seq (MACS). *Genome Biol.* **9**, R137 (2008).

958 23. Calderon, D. *et al.* Landscape of stimulation-responsive chromatin across diverse human

959 immune cells. *Nat. Genet.* **51**, 1494–1505 (2019).

960 24. Kumasaka, N., Knights, A. J. & Gaffney, D. J. Fine-mapping cellular QTLs with RASQUAL

961 and ATAC-seq. *Nat. Genet.* **48**, 206–213 (2016).

962 25. Coetzee, S. G., Coetzee, G. A. & Hazelett, D. J. motifbreakR: an R/Bioconductor package

963 for predicting variant effects at transcription factor binding sites. *Bioinforma. Oxf. Engl.* **31**,

964 3847–3849 (2015).

965 26. Kulakovskiy, I. V. *et al.* HOCOMOCO: towards a complete collection of transcription

966 factor binding models for human and mouse via large-scale ChIP-Seq analysis. *Nucleic Acids Res.*

967 **46**, D252–D259 (2018).

968 27. Pliner, H. A. *et al.* Cicero Predicts cis-Regulatory DNA Interactions from Single-Cell

969 Chromatin Accessibility Data. *Mol. Cell* **71**, 858–871.e8 (2018).

970 28. Javierre, B. M. *et al.* Lineage-Specific Genome Architecture Links Enhancers and Non-

971 coding Disease Variants to Target Gene Promoters. *Cell* **167**, 1369–1384.e19 (2016).

972 29. Grubert, F. *et al.* Genetic Control of Chromatin States in Humans Involves Local and

973 Distal Chromosomal Interactions. *Cell* **162**, 1051–1065 (2015).

974 30. Pugliese, A. Autoreactive T cells in type 1 diabetes. *J. Clin. Invest.* **127**, 2881–2891

975 (2017).

976 31. Kundu, K. *et al.* Genetic associations at regulatory phenotypes improve fine-mapping of

977 causal variants for twelve immune-mediated diseases. *bioRxiv* 2020.01.15.907436 (2020)

978 doi:10.1101/2020.01.15.907436.

979 32. Turner, A. W. *et al.* Functional Analysis of a Novel Genome-Wide Association Study

980 Signal in SMAD3 That Confers Protection From Coronary Artery Disease. *Arterioscler. Thromb.*

981 *Vasc. Biol.* **36**, 972–983 (2016).

982 33. Giambartolomei, C. *et al.* Bayesian test for colocalisation between pairs of genetic

983 association studies using summary statistics. *PLoS Genet.* **10**, e1004383 (2014).

984 34. Zhu, C. *et al.* An ultra high-throughput method for single-cell joint analysis of open

985 chromatin and transcriptome. *Nat. Struct. Mol. Biol.* **26**, 1063–1070 (2019).

986 35. Ramos-Rodríguez, M. *et al.* The impact of proinflammatory cytokines on the β -cell

987 regulatory landscape provides insights into the genetics of type 1 diabetes. *Nat. Genet.* **51**,

988 1588–1595 (2019).

989 36. Li, H. *et al.* The Sequence Alignment/Map format and SAMtools. *Bioinforma. Oxf. Engl.*

990 **25**, 2078–2079 (2009).

991 37. Korsunsky, I. *et al.* Fast, sensitive and accurate integration of single-cell data with

992 Harmony. *Nat. Methods* **16**, 1289–1296 (2019).

993 38. Li, H. & Durbin, R. Fast and accurate short read alignment with Burrows-Wheeler

994 transform. *Bioinforma. Oxf. Engl.* **25**, 1754–1760 (2009).

995 39. Quinlan, A. R. & Hall, I. M. BEDTools: a flexible suite of utilities for comparing genomic

996 features. *Bioinforma. Oxf. Engl.* **26**, 841–842 (2010).

997 40. Kent, W. J., Zweig, A. S., Barber, G., Hinrichs, A. S. & Karolchik, D. BigWig and BigBed:

998 enabling browsing of large distributed datasets. *Bioinforma. Oxf. Engl.* **26**, 2204–2207 (2010).

999 41. Ramírez, F. *et al.* deepTools2: a next generation web server for deep-sequencing data

1000 analysis. *Nucleic Acids Res.* **44**, W160–165 (2016).

1001 42. Liao, Y., Smyth, G. K. & Shi, W. The R package Rsubread is easier, faster, cheaper and
1002 better for alignment and quantification of RNA sequencing reads. *Nucleic Acids Res.* **47**, e47
1003 (2019).

1004 43. Harrow, J. *et al.* GENCODE: the reference human genome annotation for The ENCODE
1005 Project. *Genome Res.* **22**, 1760–1774 (2012).

1006 44. Greenwald, W. W. *et al.* Pgltools: a genomic arithmetic tool suite for manipulation of Hi-
1007 C peak and other chromatin interaction data. *BMC Bioinformatics* **18**, 207 (2017).

1008 45. Astle, W. J. *et al.* The Allelic Landscape of Human Blood Cell Trait Variation and Links to
1009 Common Complex Disease. *Cell* **167**, 1415–1429.e19 (2016).

1010 46. de Lange, K. M. *et al.* Genome-wide association study implicates immune activation of
1011 multiple integrin genes in inflammatory bowel disease. *Nat. Genet.* **49**, 256–261 (2017).

1012 47. Okada, Y. *et al.* Genetics of rheumatoid arthritis contributes to biology and drug
1013 discovery. *Nature* **506**, 376–381 (2014).

1014 48. Bentham, J. *et al.* Genetic association analyses implicate aberrant regulation of innate
1015 and adaptive immunity genes in the pathogenesis of systemic lupus erythematosus. *Nat. Genet.*
1016 **47**, 1457–1464 (2015).

1017 49. Jin, Y. *et al.* Genome-wide association studies of autoimmune vitiligo identify 23 new
1018 risk loci and highlight key pathways and regulatory variants. *Nat. Genet.* **48**, 1418–1424 (2016).

1019 50. Ji, S.-G. *et al.* Genome-wide association study of primary sclerosing cholangitis identifies
1020 new risk loci and quantifies the genetic relationship with inflammatory bowel disease. *Nat.*
1021 *Genet.* **49**, 269–273 (2017).

1022 51. Tin, A. *et al.* Target genes, variants, tissues and transcriptional pathways influencing
1023 human serum urate levels. *Nat. Genet.* **51**, 1459–1474 (2019).

1024 52. Bronson, P. G. *et al.* Common variants at PVT1, ATG13-AMBRA1, AHI1 and CLEC16A are
1025 associated with selective IgA deficiency. *Nat. Genet.* **48**, 1425–1429 (2016).

1026 53. Ferreira, M. A. R. *et al.* Genetic Architectures of Childhood- and Adult-Onset Asthma Are
1027 Partly Distinct. *Am. J. Hum. Genet.* **104**, 665–684 (2019).

1028 54. Purcell, S. *et al.* PLINK: a tool set for whole-genome association and population-based
1029 linkage analyses. *Am. J. Hum. Genet.* **81**, 559–575 (2007).

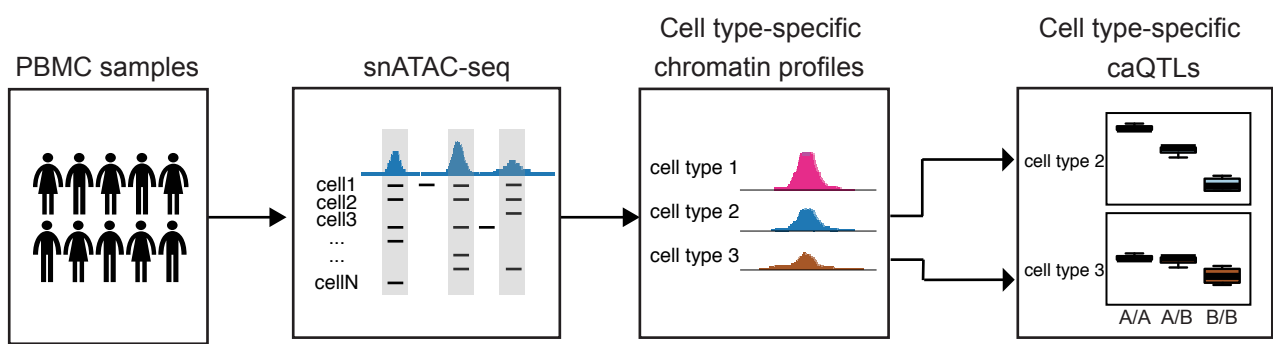
1030 55. 1000 Genomes Project Consortium *et al.* A global reference for human genetic variation.
1031 *Nature* **526**, 68–74 (2015).

1032 56. Wakefield, J. A Bayesian measure of the probability of false discovery in genetic
1033 epidemiology studies. *Am. J. Hum. Genet.* **81**, 208–227 (2007).

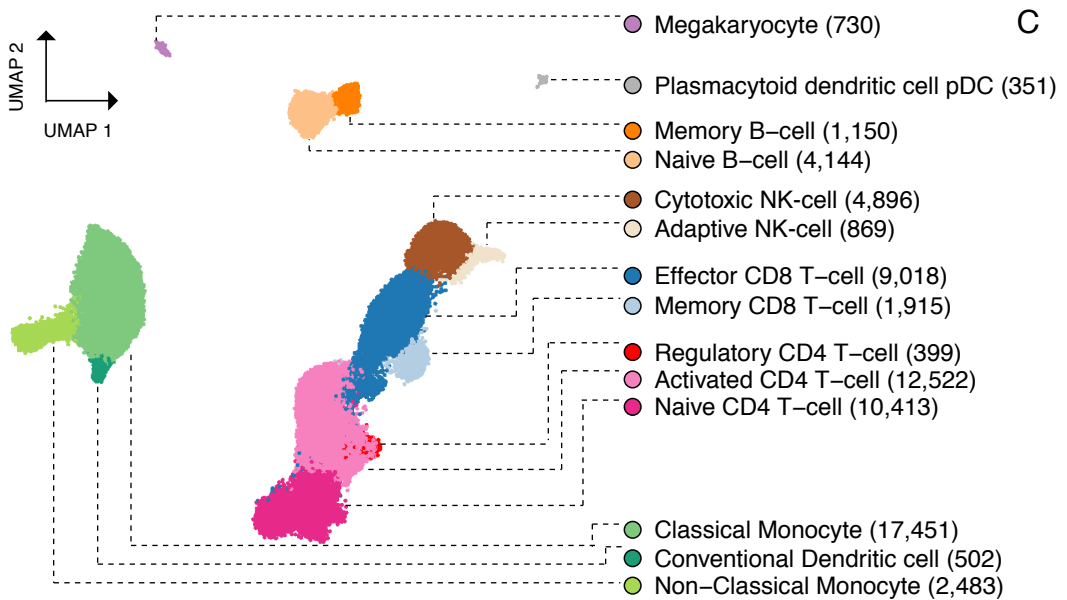
1034

1035

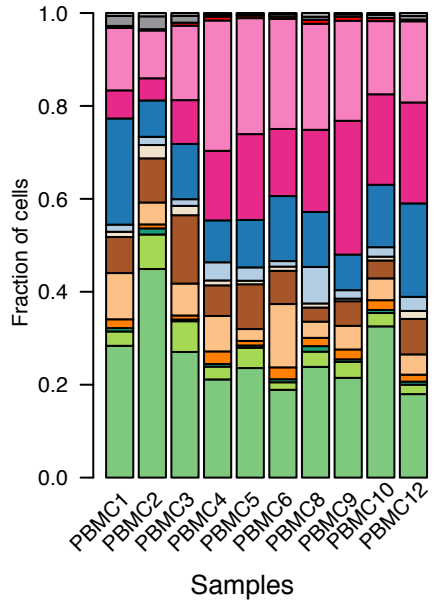
A



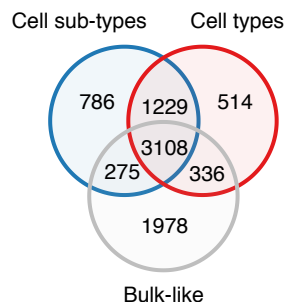
B



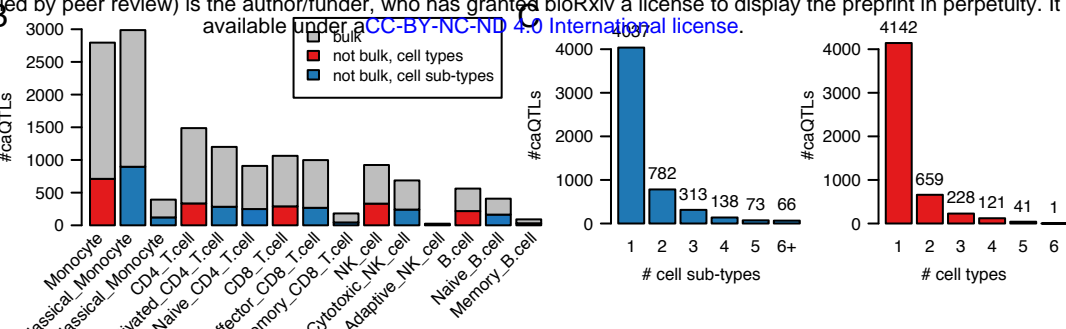
C



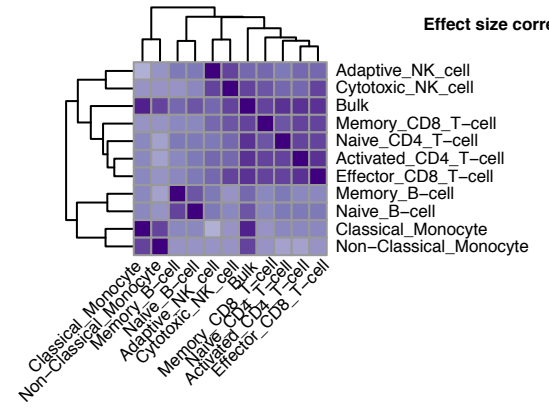
A



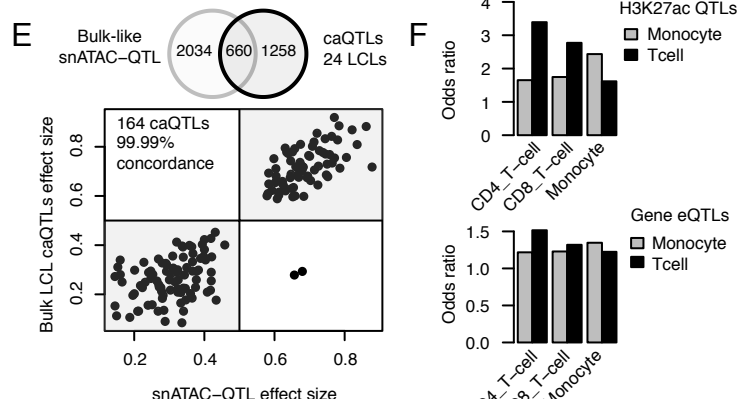
B



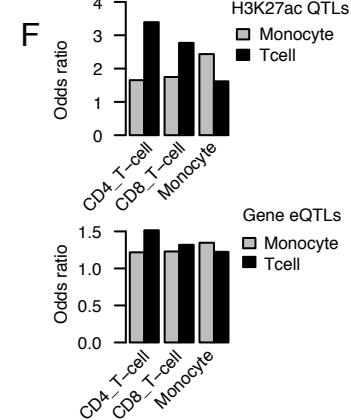
D



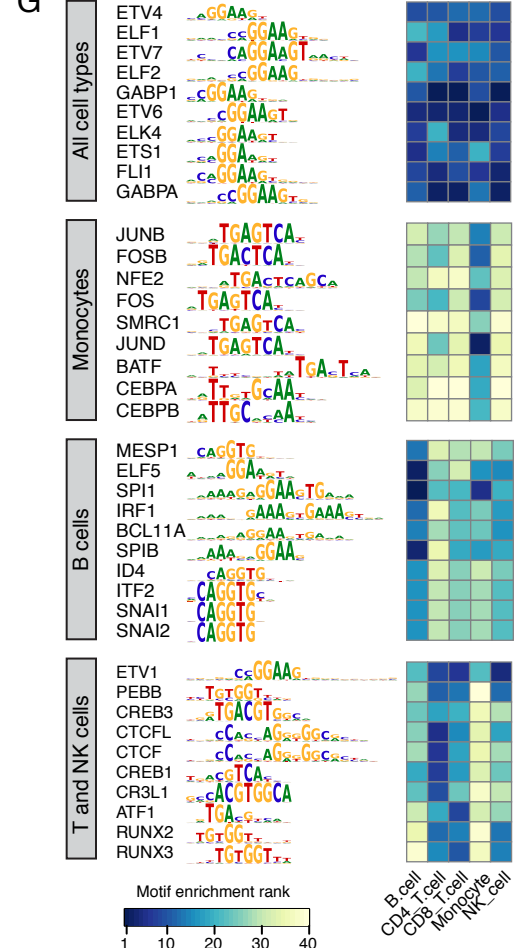
E



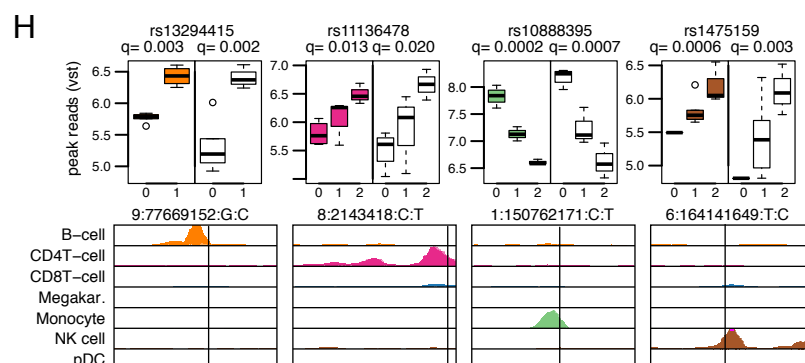
F



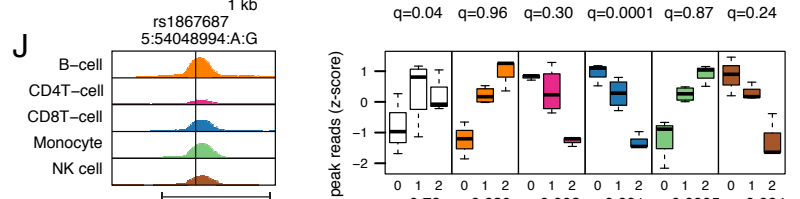
G



H



I



J

